Transition pathways between defect patterns in confined nematic liquid crystals

Yucen Han [a], Yucheng Hu [b,*], Pingwen Zhang [c,*], Lei Zhang [d,*]

[a] *Beijing International Center for Mathematical Research, Peking University, Beijing, China*
[b] *Zhou Pei-yuan Center for Applied Mathematics, Tsinghua University, Beijing, China*
[c] *Laboratory of Mathematics and Applied Mathematics, School of Mathematical Sciences, Peking University, Beijing, China*
[d] *Beijing International Center for Mathematical Research, Center for Quantitative Biology, Peking University, Beijing, China*

ARTICLE INFO

ABSTRACT

Confined nematic liquid crystals can admit multiple stable equilibria. These equilibrium states usually exhibit peculiar defect patterns in order to satisfy the topological constraints imposed by the boundary conditions. In this work, we systematically investigate transition pathways between different stable equilibria of nematic liquid crystals confined in a cylinder with homeotropic boundary condition. To do so, we implement spectral method to minimize the Landau-de Gennes free energy and develop a multiscale string method to accurately compute both minimal energy path and transition state. We first compute the transition pathways under the assumption that system state is invariant along the axial direction of the cylinder. This axial invariant assumption allows us to reduce the simulation domain to a two-dimensional disk. We subsequently remove the axial invariant assumption to search the transition pathways in the three-dimensional cylinder. Numerical simulations demonstrate that there exists a threshold for the cylinder height above which a domino-like transition pathway is more energetically favored than the axial invariant transition pathway. Moreover, we show that the transition pathway from escape radial with ring defects (ERRD) to escape radial has a lower energy barrier than the one from ERRD to planar polar, even though the free energy of the planar polar state is lower than that of the escape radial state. Our approach provides an accurate and efficient method to compute minimal energy path and transition state of confined nematic liquid crystals.

© 2019 Elsevier Inc. All rights reserved.

1. Introduction

Nematic liquid crystals are fascinating examples of complex liquids that combine fluidity with the directionality of solids, which are composed of anisotropic molecules that can possess long-range orientational order. A particularly intriguing feature of liquid crystals is topologically induced defect. Defects are discontinuities in the alignment direction of liquid crystals, and are commonly found to exist as isolated point or disclination line in experiments [1]. The existence of defect tends to increase the elastic energy of the nearby liquid crystals, and is thus not energetically favored in general. However, defects are unavoidable in some confined liquid crystal systems due to the topological constraint at the boundary. Controlled

* Corresponding authors.
  E-mail addresses: hanyc@pku.edu.cn (Y. Han), huyc@tsinghua.edu.cn (Y. Hu), pzhang@pku.edu.cn (P. Zhang), zhangl@math.pku.edu.cn (L. Zhang).

by the subtle balance between the local disorder and the topological constraint, nematic liquid crystals can exhibit various kinds of defect patterns that play an important role in the self-assembly structure and colloidal suspensions [2,3].

A topologically confined nematic liquid crystal system can admit multiple stable equilibria. These equilibrium states usually correspond to different defect patterns [4–6]. The energy landscape of the system, upon which the equilibrium states are located, is determined by the properties of the liquid crystal material as well as the environment, such as temperature, size and shape of confining space, external field, etc. Tremendous experimental and theoretical efforts have been made to investigate the defect patterns in confined nematic liquid crystals within the Landau-de Gennes model [3,7–9]. For liquid crystals confined in a cylinder with homeotropic boundary condition, it is well known that there exist at least three stable equilibria commonly known as the planar radial (PR), planar polar (PP), and escape radial (ER) [10]. The PR configuration has one disclination line with topological degree +1 in the center of the cylinder and there are two +1/2 disclination lines for the PP configuration. The ER configuration is a defect free state. All these three configurations are homogeneous along the main axis of the cylinder (axial invariant). To obtain these axial invariant configurations, it is sufficient to consider a two-dimensional (2D) disk domain (the alignment of the liquid crystals still lives in the three-dimensional (3D) domain) instead of a 3D cylinder, thus saving lots of computation power.

Under thermal fluctuation or external perturbation, the system may transit from one stable equilibrium to another, causing the position and topology of defect to change drastically [11,12]. Thus it is important, both experimentally and theoretically, to determine when and how such phase transition occurs. For the liquid crystal system with multiple stable equilibria, we want to know, which transition pathway the system would take from one stable equilibrium to another and what are the energy barrier and transition state along the transition pathway. In the zero-temperature limit, the phase transition follows the so called minimal energy path (MEP), which has the lowest energy barrier among all possible paths. The transition state corresponds to the state with the highest energy along the MEP, i.e., index-1 saddle point [13]. Extensive numerical methods have been developed to compute the MEP and transition state. For example, there are surface-walking methods such as the dimer-type methods [14,15,13,16] and path-finding methods including the nudged elastic band method [17] and the string method [18–21]. These methods have been successfully applied in nucleation and phase transformation problems in materials and soft matter [22–26].

In this work, we apply the Landau-de Gennes theory to study the transition pathways between different stable equilibria in nematic liquid crystals confined in a cylinder with homeotropic boundary condition. Numerical computation of transition pathway and transition state with high accuracy is a big challenge. First, in the Landau-de Gennes theory, the tensor order parameter has five independent variables. In addition, because the order parameter changes very rapidly near defect, we need the high spatial resolution in order to compute the free energy accurately. As a result, the spatial discretization of the order parameter is of very high dimension especially in 3D. On top of this, to compute the MEP we need to discretize the transition path, with each node in the discretized path being a tensor-field (system state). This leads to large storage space and long simulation time. To overcome these difficulties, we adapt a spectral discretization of the order parameter and develop a multiscale string method to accurately compute both MEP and transition state between two stable equilibria. We first compute the transition pathways under the axial invariant assumption, which allows us to reduce the simulation domain to a 2D disk. The computed MEP can be considered as the MEP in a constraint space in which every intermediate state along the path is axial invariant. When we remove the axial invariant assumption and carry out full 3D simulation, the MEP connecting two axial invariant equilibria may break the axial invariant property. By comparing the energy barriers of the MEPs with and without the axial invariant assumption, we find that the axial invariant MEP is more energetically favored only when the height of the cylinder is relatively small. As the height of cylinder increases, a domino-like phase transition in the 3D domain has a lower energy barrier than the axial invariant one.

The rest of this paper is organized as follows: In Section 2, we introduce the Landau-de Gennes theory for nematic liquid crystals confined in a cylinder subject to homeotropic boundary condition. In Section 3, we present the spectral method and the multiscale string method to compute the MEP and the transition state. Numerical results are presented and discussed in Section 4, and some concluding remarks are made in Section 5.

2. Landau-de Gennes theory

The Landau-de Gennes theory [1] is capable of describing nematic-isotropic phase transition in liquid crystals. The order parameter of the liquid crystal in the Landau-de Gennes theory is represented by $\mathbf{Q}$-tensor, which is a symmetric, traceless second-rank tensor that can be written as

$$\mathbf{Q} = \lambda_1 \mathbf{n}_1 \otimes \mathbf{n}_1 + \lambda_2 \mathbf{n}_2 \otimes \mathbf{n}_2 + \lambda_3 \mathbf{n}_3 \otimes \mathbf{n}_3. \tag{1}$$

Here $\lambda_1, \lambda_2, \lambda_3$ ($\lambda_1 \geq \lambda_2 \geq \lambda_3$) are eigenvalues and $\mathbf{n}_1, \mathbf{n}_2, \mathbf{n}_3$ are the corresponding unit eigenvectors. Because $\mathbf{Q}$ is traceless, i.e., $\sum_{i=1}^{3} \lambda_i = 0$, it can be also written as

$$\mathbf{Q} = s\left(\mathbf{n}_1 \otimes \mathbf{n}_1 - \frac{\mathbf{I}}{3}\right) + r\left(\mathbf{n}_2 \otimes \mathbf{n}_2 - \frac{\mathbf{I}}{3}\right), \ s, r \in \mathbb{R}, \ \mathbf{n}_1, \mathbf{n}_2 \in \mathbb{S}^2, \tag{2}$$

where $s = \lambda_1 - \lambda_3 = 2\lambda_1 + \lambda_2$ and $r = \lambda_2 - \lambda_3 = \lambda_1 + 2\lambda_2$. When $s = 0$ and $r = 0$, or equivalently, $\lambda_1 = \lambda_2 = \lambda_3 = 0$, $\mathbf{Q}$ is isotropic. When $s \neq 0$ and $r = 0$ (or $s = 0$ and $r \neq 0$), $\mathbf{Q}$ is uniaxial, in which case $\mathbf{Q}$ can be expressed as $s\left(\mathbf{n}_1\mathbf{n}_1 - \frac{\mathbf{I}}{3}\right)$ (or $r\left(\mathbf{n}_2\mathbf{n}_2 - \frac{\mathbf{I}}{3}\right)$). When $s \neq 0$ and $r \neq 0$ ($\lambda_1 \neq \lambda_2 \neq \lambda_3$), $\mathbf{Q}$ is biaxial.

In the absence of boundary constraint and external field, the Landau-de Gennes free energy is given by

$$F[\mathbf{Q}] = \int_{\Omega} [f_b(\mathbf{Q}) + f_{el}(\mathbf{Q})]\mathrm{d}V. \tag{3}$$

The bulk energy density is defined as [1,27]

$$f_b(\mathbf{Q}) = \frac{A}{2}\mathrm{tr}(\mathbf{Q}^2) - \frac{B}{3}\mathrm{tr}(\mathbf{Q}^3) + \frac{C}{4}\mathrm{tr}(\mathbf{Q}^2)^2. \tag{4}$$

Here A, B, C are the material-dependent constants. A is linearly dependent with temperature, i.e., $A = \alpha(T - T^*)$, where T^* is the characteristic liquid crystal temperature below which the isotropic state becomes unstable. The elastic energy density consists of the three quadratic terms in the first partial derivatives of $\mathbf{Q}$ which are invariant under rigid rotations. Specifically,

$$f_{el}(\mathbf{Q}) = \frac{L_1}{2}\mathbf{Q}_{ij,k}\mathbf{Q}_{ij,k} + \frac{L_2}{2}\mathbf{Q}_{ij,j}\mathbf{Q}_{ik,k} + \frac{L_3}{2}\mathbf{Q}_{ij,k}\mathbf{Q}_{ik,j}, \tag{5}$$

where $\mathbf{Q}_{ij,k} = \frac{\partial \mathbf{Q}_{i,j}}{\partial x_k}$ and L_1, L_2, L_3 are elastic constants. The elastic energy penalizes spatial non-homogeneities. In the following we assume $L_2 = L_3 = 0$, which is the simplest form of elastic energy [28,29].

In this work we consider liquid crystals confined in a cylinder Ω with radius R and height H. To nondimensionalize the Landau-de Gennes free energy, we define

$$A_{NI} = \frac{B^2}{27C}, \quad t = \frac{27AC}{B^2} = \frac{A}{A_{NI}}, \tag{6}$$

where A_{NI} denotes the transition value of nematic-isotropic bulk energy and t is the reduced temperature. The nematic-isotropic transition temperature is adjusted to $t = 1$. $t = 0$ is the critical temperature below which the isotropic phase is unstable and $t = \frac{9}{8}$ is super heating limit above which the nematic phase is unstable. The characteristic length and corresponding dimensionless radius and height are

$$\xi_0 = \sqrt{\frac{L_1}{A_{NI}}} = \sqrt{\frac{27CL_1}{B^2}}, \quad \bar{R} = \frac{R}{\xi_0}, \quad \bar{H} = \frac{H}{\xi_0}. \tag{7}$$

After rescaling variables as

$$\bar{\mathbf{Q}} = \sqrt{\frac{27C^2}{2B^2}}\mathbf{Q}, \quad \bar{F} = \sqrt{\frac{27C^3}{4B^2L_1^3}}F,$$

the Landau-de Gennes free energy becomes (after dropping the bars for simplicity),

$$F[\mathbf{Q}] = \int_{\Omega} [\frac{t}{2}\mathrm{tr}(\mathbf{Q}^2) - \sqrt{6}\mathrm{tr}(\mathbf{Q}^3) + \frac{1}{2}\mathrm{tr}(\mathbf{Q}^2)^2 + \frac{1}{2}\mathbf{Q}_{ij,k}\mathbf{Q}_{ij,k}]\mathrm{d}V. \tag{8}$$

Typical values of parameters are $\alpha = 0.14 \times 10^6$ J/m$^3 \cdot$ K, $T^* = 34.2°$C, $B = 1.8 \times 10^6$ J/m^3, $C = 3.6 \times 10^6$ J/m^3, $L_1 = 3.0 \times 10^{-12}$J/m, and $\xi_0 = 9.5 \times 10^{-9}$ m [30].

We consider homeotropic boundary condition at the lateral surface Γ of the cylinder Ω (liquid crystals tend to point in the direction perpendicular to the lateral surface) and periodic boundary condition at the top and bottom caps of the cylinder. This boundary condition is modeled as an extra penalty term in the total free energy:

$$\int_{\Gamma} f_s(\mathbf{Q})ds = \int_{\Gamma} \omega|\mathbf{Q} - \mathbf{Q}_0|^2 ds, \tag{9}$$

where $\mathbf{Q}_0 = s_0(\mathbf{n} \otimes \mathbf{n} - \frac{\mathbf{I}}{3})$ is the minimizer of the bulk energy part in Eq. (8), with $s_0 = \sqrt{\frac{3}{2}} \cdot \frac{3+\sqrt{9-8t}}{4}$. $\mathbf{n}$ is the perpendicular direction of the lateral surface of the cylinder, i.e., $\mathbf{n} = (\cos(\phi), \sin(\phi), 0)$. To mimic the Dirichlet boundary condition we use a very large boundary coefficient $\omega = 10^5$ in our simulations.

3. Computational methods

3.1. Spectral expansion method

The symmetric traceless tensor has five degrees of freedom and can be written as

$$\mathbf{Q} = \begin{bmatrix} q_1 & q_2 & q_3 \\ q_2 & q_4 & q_5 \\ q_3 & q_5 & -q_1 - q_4 \end{bmatrix}. \tag{10}$$

We rescale the simulation domain Ω to $D_1 \times [0, 2\pi]$ and expand $\mathbf{Q}$ using the Zernike polynomials [31,32].

We first assume that $\mathbf{Q}$ is invariant along the z-axis. So the minimization of the free energy can be reduced to a 2D disk and the expansion of $\mathbf{Q}$ by the 2D Zernike polynomials is written as

$$q_i(r, \phi) \approx \sum_{l=1-L}^{L-1} \sum_{n=|l|}^{N-1} A_{nl}^{(i)} Z_{nl}(r, \phi), \ \ 0 \le r \le 1, \ \ 0 \le \phi < 2\pi,$$

where

$$\begin{aligned} Z_{nl}(r, \phi) &= R_n^{(|l|)}(r) X_l(\phi), \\ R_n^{(l)} &= \begin{cases} \sum_{s=0}^{(n-l)/2} N_{nls} r^{n-2s} & 0 \le \frac{n-l}{2} \in \mathbb{Z}, \\ 0 & \text{otherwise}, \end{cases} \\ N_{nls} &= (-1)^s \sqrt{2n+2} \frac{(n-s)!}{s! (\frac{n+l}{2} - s)! (\frac{n-l}{2} - s)!}, \\ X_l(\phi) &= \begin{cases} \frac{1}{\pi} \cos l\phi & l > 0, \\ \frac{1}{2\pi} & l = 0, \\ \frac{1}{\pi} \sin |l|\phi & l < 0. \end{cases} \end{aligned}$$

In numerical simulations, we choose the truncation orders to be $N = L = 64$. Note that relatively large truncation orders are needed because Q changes very rapidly near the disclination lines.

If we remove the axial invariant assumption and consider full 3D, the periodic boundary condition requires that $\mathbf{Q}(x, y, 0) = \mathbf{Q}(x, y, 2\pi)$ and $\mathbf{Q}$ is expanded by the 3D Zernike polynomials coupled with the Fourier series as

$$q_i(r, \phi, z) \approx \sum_{m=1-M}^{M-1} \sum_{l=1-L}^{L-1} \sum_{n=|l|}^{N-1} A_{nlm}^{(i)} Z_{nl}(r, \phi) X_m(z),$$

$$0 \le r \le 1, \ \ 0 \le \phi < 2\pi, \ \ 0 \le z \le 2\pi,$$

where the truncation orders are $N = L = 64$ and $M = 16$.

We apply the Limited-memory BFGS (L-BFGS) [33] to minimize the Landau-de Gennes free energy for finding the stable equilibria of nematic liquid crystals. Given a random initial state, we claim that the system reaches a stable equilibrium and stop the iteration when the L_2-norm of the gradient of the Landau-de Gennes free energy is sufficiently small (10^{-5}).

3.2. Multiscale string method

To compute the MEP and the transition state, we develop a multiscale string method. The string method was first proposed by E, Ren and Vanden-Eijnden [19] and has some variants [18,20,21,34]. Denote by $F(x)$ the potential energy of the system, the string method to find the MEP is to evolve a string ϕ by using the steepest descent dynamics:

$$\phi_t = -\nabla F^{\perp}(\phi) + \lambda \tau, \tag{11}$$

where $\nabla F^{\perp}(\phi)$ is the component of ∇F normal to ϕ, τ denotes the unit tangent vector to ϕ, and λ is the Lagrange multiplier to impose the equal arc-length constraint.

In the numerical algorithm, the string ϕ is discretized to a number of nodes $\{\mathbf{Q}_i^n, i = 1, .., N\}$, where n is the iteration step of the numerical algorithm and N is the number of the nodes. Then the string method adopts a time splitting scheme via the following two-step procedure:

First is the string evolution step. In the classical string method [19], the current path $\{\mathbf{Q}_i^n, i = 1, .., N\}$ is updated by following the gradient decent direction:

$$\bar{\mathbf{Q}}_i^{n+1} = \mathbf{Q}_i^n - \alpha_i \nabla F^{\perp}[\mathbf{Q}_i^n], \quad i = 1, 2, \cdots, N, \tag{12}$$

where α_i is a stepsize that is chosen as a constant or determined by the linesearch.

Since the evolution step can be formulated as a minimization procedure [34], it can be solved by efficient optimization algorithms for better convergence. Here, we implement the L-BFGS algorithm for better convergence. Starting with $\phi_0 = \mathbf{Q}_i^n$, the L-BFGS scheme iterates the following steps until convergence is achieved:

1. Compute the searching direction $p_k = -\mathbf{H}_k \nabla F(\phi_k)$ and update the string $\phi_{k+1} = \phi_k + \alpha_k \bar{p}_k$, where α_k is chosen by the linesearch and $\bar{p}_k$ is the projection of p_k perpendicular to the tangent direction of the string τ_k;
2. Update the approximation of the inverse Hessian

$$\mathbf{H}_{k+1} = \mathbf{H}_k + \frac{s_k s_k{}^T}{y_k{}^T s_k}\left(\frac{y_k{}^T \mathbf{H}_k y_k}{y_k{}^T s_k} + 1\right) - \frac{1}{y_k{}^T s_k}(s_k y_k{}^T \mathbf{H}_k + \mathbf{H}_k y_k s_k{}^T)$$

where $s_k = \alpha_k p_k$ and $y_k = \nabla F(\phi_{k+1}) - \nabla F(\phi_k)$.

In practice, we found the projection $\bar{p}_k$ can be replaced by the searching direction p_k to improve the stability and convergence in the same manner as the simplified string method [20].

The second step is the string reparametrization. The simplest way is to enforce the equal arc-length parametrization: one can calculate the arc length corresponding to the current nodes $\bar{\mathbf{Q}}_i^{n+1}$ and then use a linear or cubic spline interpolation to obtain the new nodes $\mathbf{Q}_i^{n+1}$ by equal arc length.

Parametrization by equal arc length gives a good accuracy for the MEP, but not for the transition state. To achieve the better estimation of the transition state, one way is to use energy-weighted arc length so that finer resolution can be achieved around the transition state [20]. If the final minimum is far from the transition state, the free-end nudged elastic band method can be used to obtain subtle depiction around the transition state by allowing the last node not to be a minimum [35].

To improve the accuracy of both MEP and transition state without using too many nodes, we propose a multiscale scheme of the string method by applying both a global coarse string and a local fine string. The global coarse string is used to obtain the whole MEP by connecting two minima, and the local fine string is utilized to compute the local MEP by choosing two nodes with the highest energies on the global coarse string as two ends. Both strings follow the same two-step procedure described above to make the implementation straightforward, and better estimation of the transition state can be achieved by the local fine string. In practice, we may need a second local string between the highest energy node and the other neighbor if the first local string missed the energy barrier. We will perform numerical simulations by the multiscale string method for 3D transition pathways because of expensive computational cost in 3D. Such multiscale scheme of the string method can be naturally extended for the multi-barrier crossing events [20].

4. Results

For visualization purpose, we use ellipsoids to represent the $\mathbf{Q}$-tensors. The semi-axises of the ellipsoids d_1, d_2 and d_3 ($d_1 \geq d_2 \geq d_3$) correspond to the three eigenvalues of $\mathbf{Q}$ by $d_1 = \lambda_1 + 1/3$, $d_2 = \lambda_2 + 1/3$ and $d_3 = \lambda_3 + 1/3$. To visualize biaxiality, we define β as

$$\beta = 1 - 6\frac{(tr\mathbf{Q}^3)^2}{(tr\mathbf{Q}^2)^3}. \tag{13}$$

$\beta = 0$ if $\mathbf{Q}$ is uniaxial. $\beta = 1$ corresponds to the case that biaxiality is maximal [36].

In addition, we introduce the Westin metric [37]

$$c_l = d_1 - d_2, \tag{14}$$

and use the isosurface of c_l to represent the disclination lines.
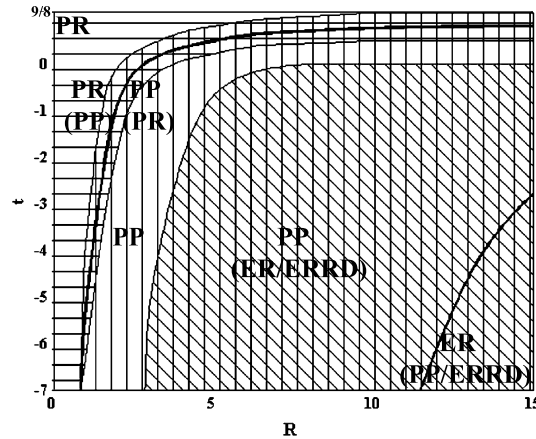
4.1. Phase diagram

First, we apply the L-BFGS algorithm to minimize the Landau-de Gennes free energy and four stable equilibria of nematic liquid crystals confined in a cylinder with homeotropic boundary condition can be found, as shown in Fig. 1. The PR configuration (Fig. 1(a)) is axial invariant and radial symmetry. The principal eigenvector of $\mathbf{Q}$ is parallel to the transverse section and perpendicular to lateral boundary. It contains one $+1$ disclination line in the center of cylinder. The PP configuration (Fig. 1(b)) is also axial invariant but does not maintain radial symmetry. There are two $+1/2$ disclination lines inside the cylinder. The ER configuration (Fig. 1(c)) is axial invariant and radial symmetry, but contains no defect. The escape radial with ring defect (ERRD) configuration (Fig. 1(d)) has two disclination rings lying on a plane parallel to the axial direction of the cylinder. Two disclination rings can be considered as the broadening of two point defects with topological charge $+1$ and -1 [38]. The ERRD solution can be considered as a quenched metastable state formed by jointing ER configurations with opposite pointing directions, which means the free energy of ERRD is always higher than ER.

To study the parameter regions in which different defect patterns are stable, we plot the phase diagram for different temperature t and radius R in Fig. 2. The PR configuration is the state with the lowest free energy for temperature close to
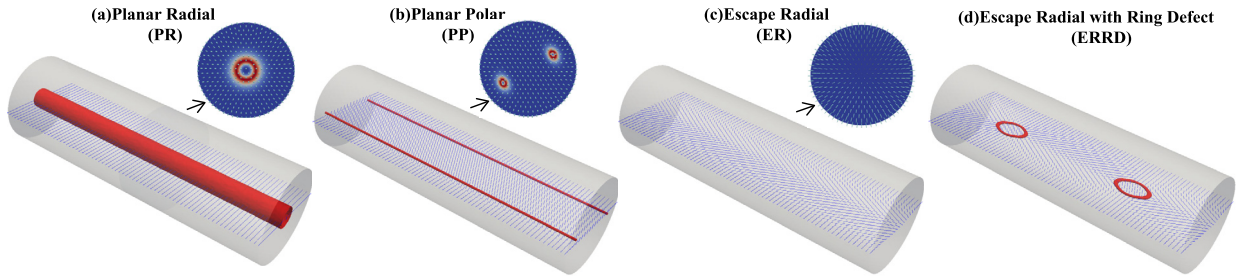
Fig. 1. Four equilibria of nematic liquid crystal confined in cylinder. Disclination lines are represented by the red isosurface of c_l in Eq. (14). The disk in the upper-right corner is the transversal view of structure in (a)–(c). The ellipsoid on disk represents the **Q**-tensor on the disk and the color corresponds to β in Eq. (13), ranging from 0 (blue) to 1 (red). (For interpretation of the colors in the figure(s), the reader is referred to the web version of this article.)

Fig. 2. Phase diagram of the PR, PP, ER and ERRD configurations. The domain is divided into three parts and separated by black bold lines according to the lowest energy of PR, PP and ER. Stable regions of PR, PP and ER are filled with horizontal line, vertical line, and oblique line, respectively. In the overlapping regions, two or three configurations are stable and the configurations indicated in parentheses have higher energy.

isotropic-nematic phase transition and small radius. As temperature decreases and radius increases, the energy difference between PP and PR is smaller. When temperature is low and radius is large, ER becomes the state with the lowest free energy. There is a region where both PR and PP are stable surrounding the line separating stable PR and PP configurations. The PP, ER and ERRD configurations are all stable around the line separating stable PP and ER, and ERRD is always stable but has relatively higher energy. This phase diagram is consistent with the previous findings [39,40]. We refer to [40] for more discussions about the PR, PP, ER and ERRD structures.

4.2. Transition pathways

Next, we study the transition pathways between different defect patterns in Fig. 1. The MEP from PR to PP is shown in Fig. 3(e). During the phase transition process, we can see that the +1 disclination line (now is a +1 point defect in 2D disk (Fig. 3(a))) gradually splits into two +1/2 disclination lines (two +1/2 point defects in 2D disk (Fig. 3(d))). The node with the highest energy on the MEP corresponds to the transition state (Fig. 3(c)). Before reaching this transition state, the free energy increases as the distance between two disclination lines increases. However, after reaching a critical distance the free energy begins to drop as the distance between two disclination lines continues to increase. The last few nodes along the MEP stay flat because energy differences among these nodes are relatively small. This suggests that, when two disclination lines are far away from each other, the change of their distance has little effect on the free energy of the system.

We compare the MEPs from PR to PP for different t and R in Fig. 4. The energy values of the PR configurations at different t are shifted to zero for comparison. When t decreases from 0.86 to 0.84 for fixed $R = 5$ (Fig. 4(a)), the energy difference between PR and PP increases as the system favors the PP configuration at a low temperature. Meanwhile, the energy barrier (the maximum energy on the MEP minus the energy of PR) decreases, indicating the transition from PR to PP becomes easier at a low temperature. Similarly, if the temperature t is fixed, we observe an increase of the energy difference between PR and PP and a decrease of the energy barrier as R increases (Fig. 4(b)).

We also compute the MEP from ER to PP in Fig. 5. Starting from the ER (Fig. 5(a)), the transition pathway goes thorough a transition state in which two separated +1/2 disclination lines start to separate (Fig. 5(b)). This transition state is quite different compared with that from PR to PP where a similar configuration (Fig. 3(b)) is still insufficient to overcome the energy barrier. In Fig. 5(b)–(d), the distance of two +1/2 disclination lines is getting further. Then, we compare MEPs from
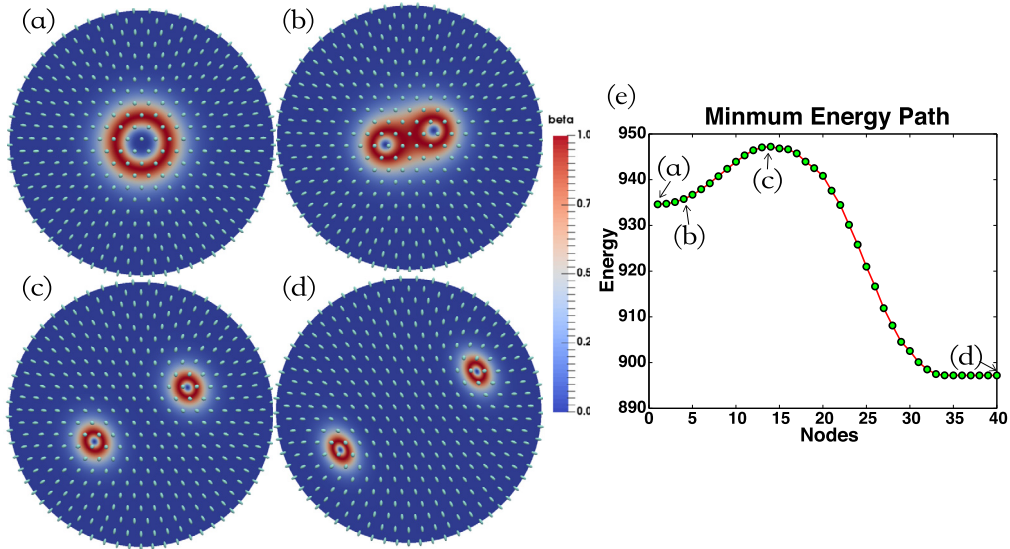
Fig. 3. Transition pathway from PR to PP with $t = 0.85$ in Eq. (6) and $R = 5$ in Eq. (7). (a)–(d) Transversal view of configurations along the MEP (e), corresponding to the PR (a), an intermediate state (the 4th node) (b), the transition state (c) and the PP (d), respectively. The ellipsoid represents the **Q**-tensor on the disk and the color corresponds to β in Eq. (13), ranging from 0 (uniaxial) to 1 (biaxial).
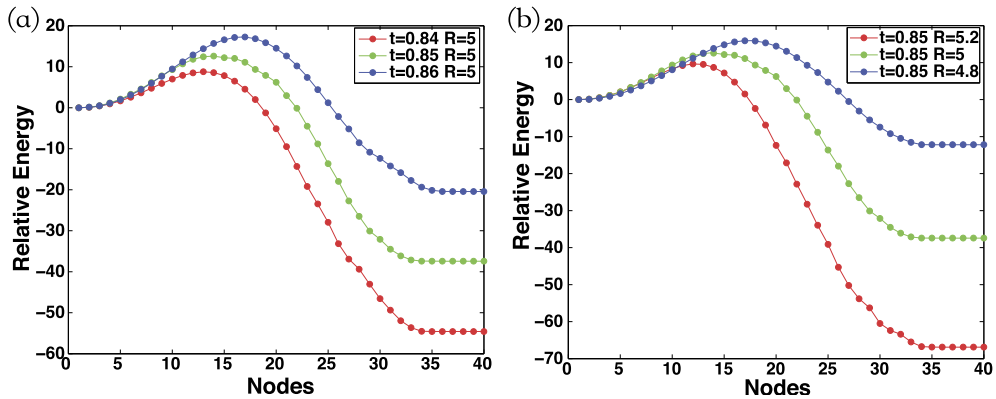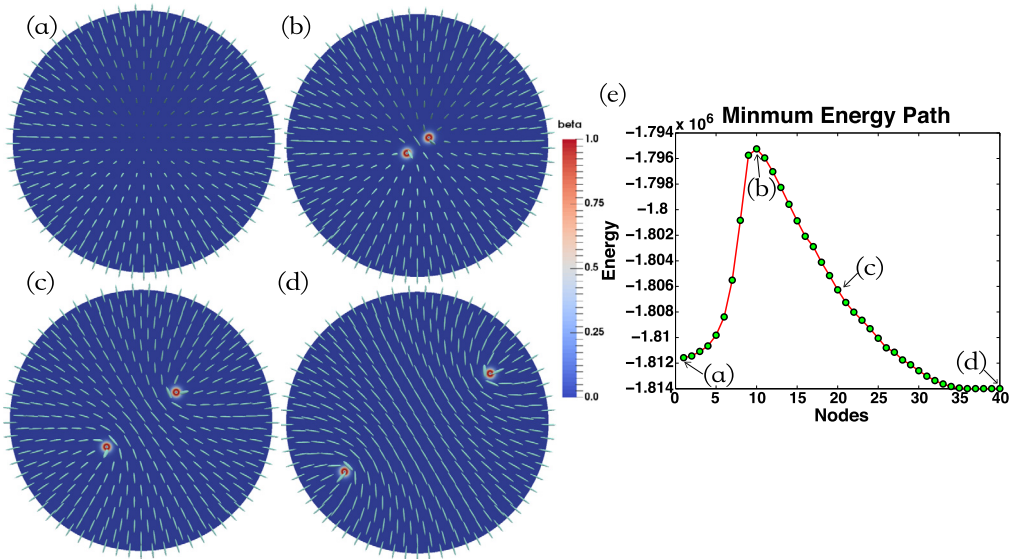

Fig. 4. MEPs from PR to PP configuration for the homeotropic boundary condition as t or R changes. (a) Relative energy change along the MEPs for different t. (b) Relative energy change along the MEPs for different R.

ER to PP for different values of t and R in Fig. 6. For $R = 13$, as the temperature decreases the energy difference between ER and PP decreases, while the energy barrier increases, suggesting that the transition from ER to PP gets harder and the configuration of ER becomes more stable. On the other hand, we can increase the domain radius R to decrease the energy difference between ER and PP and increase the energy barrier.

So far we have transition pathways that are axial invariant between two axial invariant configurations. However, it is unclear whether the transition pathway can break such axial invariance. To answer it, we remove the axial invariant assumption and compute the MEP in the full 3D space. In order to accurately compute both the MEP and the transition state simultaneously without using too many nodes on the string, we implemented the multiscale string method by applying a global coarse string and a local fine string in 3D simulations.

We compute the MEP from PR to PP without the axial invariant assumption and obtain the transition pathway as shown in Fig. 7. We can see that the phase transition starts with the splitting of the $+1$ disclination line into two $+1/2$ disclination lines in the middle of the cylinder (Fig. 7(b)). At first, the split region is small, and the width of splitting region increases until it reaches the distance between two $+1/2$ disclination lines of PP. Meanwhile, the split region gradually extends along the main axial of the cylinder in both sides, until finally reaching the boundaries. If we only look at any transversal section of the cylinder, the phase transition is very similar with the axial invariant one shown in Fig. 3. The major difference here is now the splitting process does not occur simultaneously, but propagates from the middle of the cylinder to both ends, like a falling row of dominoes.

Since we have uncovered two different MEPs from PR to PP—one that is axial invariant and the other that is not, it is natural to ask which MEP has lower energy barrier and hence is more energetically favorable. In the limit of the cylinder

Fig. 5. Transition pathway from ER to PP with $t = -6$ and $R = 10$. (a)–(d) Four transversal view of configurations along the MEP (e), corresponding to the ER (a), the transition state (b), an intermediate state (the 20th node) (c), and the PP (d), respectively.
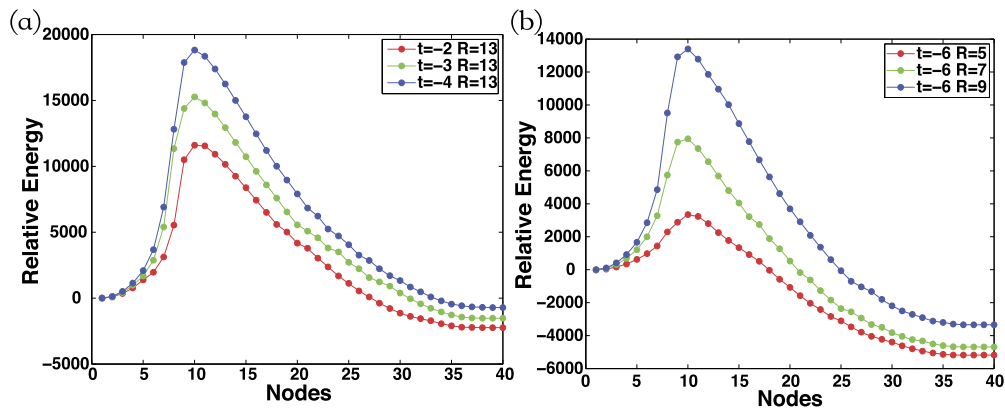

Fig. 6. MEPs from ER to PP configuration with homeotropic boundary condition as t or R changes. (a) Relative energy change along the MEPs for different t. (b) Relative energy change along the MEPs for different R.

height approaches to zero, the cylinder becomes a disk and the axial invariant MEP should have lower energy barrier. On the other hand, in the limit of infinitely long cylinder, it will cost infinite energy to separate two disclination lines in parallel. So the axial invariant MEP should have infinitely large energy barrier. To check the dependence of energy barrier on cylinder height, we calculate the energy barriers of the axial invariant MEPs and the MEPs with ring defect (without axial invariant) for different cylinder heights in Fig. 8. Indeed, there exists a threshold value of cylinder height H^*, so that the MEP with ring defect has lower energy barrier when $H > H^*$. Moreover, this energy barrier approaches to a constant as the cylinder height increases. This result is consistent with the domino effect, a cumulative effect produced when one event initiates a succession of similar events. The energy barrier is only determined by the critical push (i.e. the transition state), but not the length of the reaction chain. Thus, for long enough cylinder, the transition dynamics would follow a domino-like process, and its energy barrier does not depend on the cylinder height H.

In comparison with the axial invariant MEP from ER to PP, the new MEP without axial invariant assumption also looks like a domino-like process (Fig. 9). In particular, a pair of $+1/2$ disclination lines starts to form in the middle of the cylinder. These two disclination lines appear to join their both ends, hence forming a disclination ring (Fig. 9(b)).

Up to now we have only considered MEPs connecting two stable equilibria that are both axial invariant. There exists stable equilibrium that is not axial invariant, for example, the ERRD configuration as shown in Fig. 1(d). Thus to study MEP involving ERRD, full 3D simulation must be used. In a certain parameter region, ERRD, ER and PP are all stable and ERRD has higher energy than ER and PP. It is interesting to investigate transition pathways from ERRD to either ER or PP and find out which pathway is more probable. In Fig. 10, we compute the MEPs from ERRD to ER and from ERRD to PP by setting $t = -6$, $R = 10$, and $H = 20\pi$. The transition pathway from ERRD to ER is shown in Fig. 10(a)–(d). Two
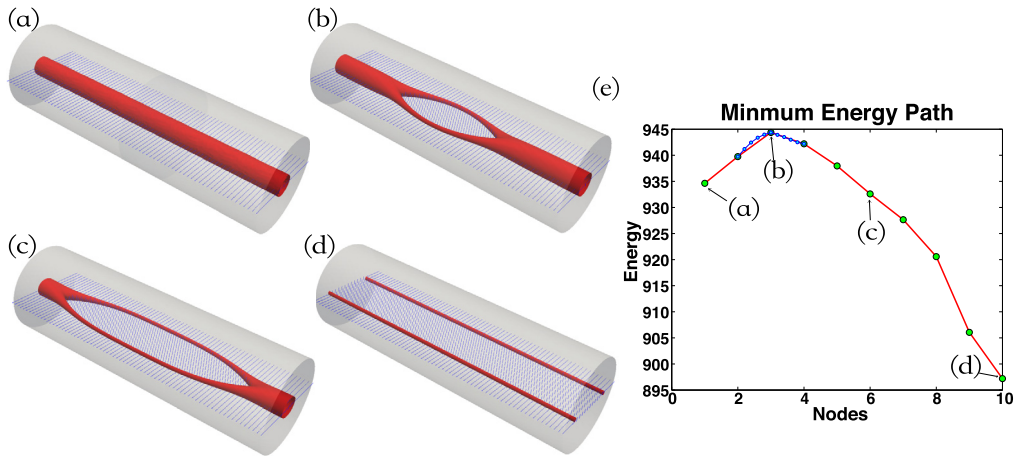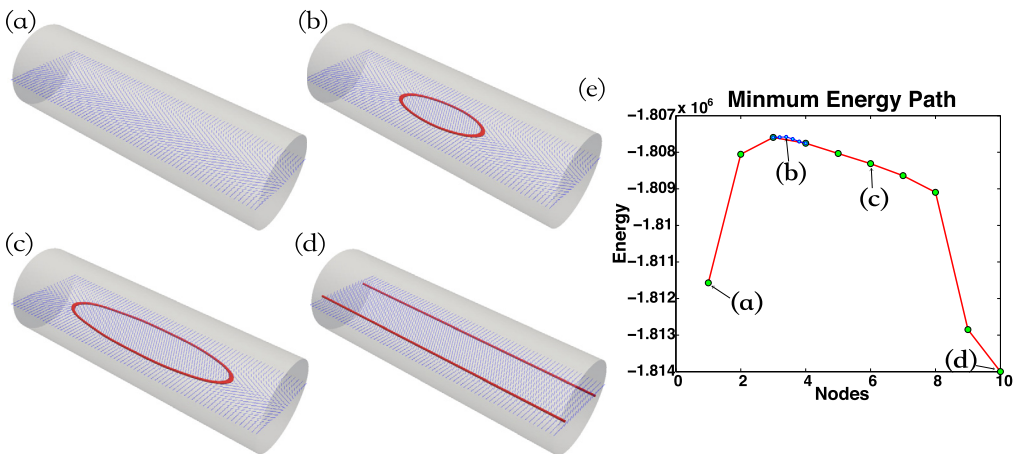
Fig. 7. Transition pathway from PR to PP with $t = 0.85$, $R = 5$ and $H = 10\pi$. (a)–(d) Four states along the MEP (e), corresponding to the PR (a), the transition state (b), an intermediate state (c), and the PP (d), respectively. In the MEP(e), the red line with green beads is the global coarse string and the blue line with blue beads is the local fine string.
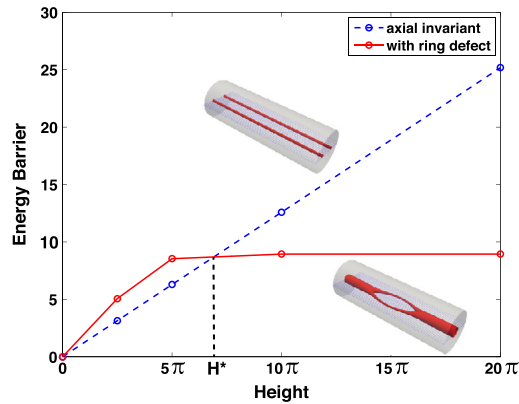
Fig. 8. Energy barrier from PR to PP vs cylinder height. $t = 0.85$ and $R = 5$. The axial invariant transition state and the transition state with ring defect are inserted for illustration.

Fig. 9. Transition pathway from ER to PP with $t = -6$, $R = 10$, and $H = 20\pi$. (a)–(d) Four states along the MEP (e), corresponding to the ER (a), the transition state (b), an intermediate state (the 6th node) (c), and the PP (d), respectively. In the MEP(e), the red line with green beads is the global coarse string and the blue line with blue beads is the local fine string.
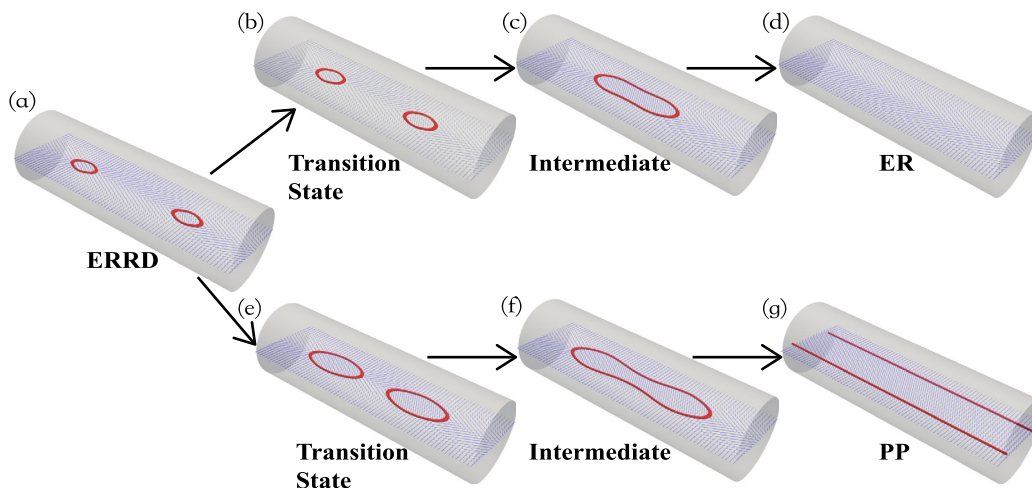
Fig. 10. Two transition pathways starting from ERRD. (a)–(d) describe transition pathway from ERRD to ER. (a) and (d) are equilibria. (b) is transition state and (c) is intermediate. (a), (e)–(g) describe transition pathway from ERRD to PP. (a) and (g) are equilibria. (e) is transition state and (g) is intermediate. $t = -6$, $R = 10$, $H = 20\pi$.

disclination rings first move towards each other (Fig. 10(b)). While two disclination rings approach each other, their sizes do not change significantly. Eventually, two rings collide and merge into one hourglass-shaped disclination ring (Fig. 10(c)). The newly formed disclination ring will shape to be an ellipse (similar to Fig. 8(b)) and which will gradually shrink in size and eventually vanish. The transition path from ERRD to PP is shown in Fig. 10(a), (e)–(g). We can see that, unlike the previous transition process, now two disinclination rings enlarge their sizes but maintain their position. As two disclination rings elongate along the axial direction, eventually merge into one disclination ring, and form as structure similar to Fig. 8(c). Finally, the merged ring continues to elongate to form the PP configuration.

It is also interesting to know that under the current parameter setting, PP has the lowest energy and ERRD has the highest energy ($E_{PP} = -1.813 \times 10^6$, $E_{ER} = -1.811 \times 10^6$, $E_{ERRD} = -1.804 \times 10^6$). However, the energy barriers of ERRD to ER and ERRD to PP are 79.55 and 319.41, respectively. Thus, the transition pathway from ERRD to ER is more likely to happen because its energy barrier is lower than the other one from ERRD to PP, even though PP is more stable than ER.

5. Conclusions

In this work, we apply the Landau-de Gennes theory to study transition pathways between defect patterns of nematic liquid crystals confined in a cylinder with homeotropic boundary condition. We propose a multiscale string method coupled with spectral method to compute both MEP and transition state more accurately and efficiently. The MEP provides detailed information of the transition dynamics, and the transition state gives the critical configuration in phase transition and determines the energy barrier on the MEP.

We first assume the invariance of system state along the z-axis so that we can reduce the computational domain from 3D cylinder to 2D disk. We compute the transition pathways from PR to PP and from ER to PP and show how the energy barrier changes with the temperature and the system size. These findings are crucial for the design of sensors based on the phase transition of confined liquid crystals. We subsequently remove the axial invariant assumption and carry out full 3D simulation in a cylinder to search the transition pathways that may break the axial invariance. Our simulations demonstrate that a domino-like transition pathway has lower energy barrier than the axial invariant transition pathway when the cylinder height is larger than a critical value, which reveals the importance of geometry size on the transition dynamics of nematic liquid crystals.

Our methods can be naturally extended to more complex geometries and boundary conditions, such as liquid crystals confined in a 3D droplet under homeotropic or planar anchoring conditions [39]. There are other numerical methods that directly simulate the transition dynamics of liquid crystal [41], which may advance our understanding of the design of liquid crystal devices that utilizes the transition processes between stable equilibria.

Acknowledgements

References

[1] P.G. de Gennes, J. Prost, The physics of liquid crystals, vol. 83, Oxford university press, 1995.
[2] G. Foffano, J.S. Lintuvuori, A. Tiribocchi, D. Marenduzzo, The dynamics of colloidal intrusions in liquid crystals: a simulation perspective, Liq. Cryst. Rev. 2 (1) (2014) 1–27.
[3] I. Muševič, M. Škarabot, U. Tkalec, M. Ravnik, S. Žumer, Two-dimensional nematic colloidal crystals self-assembled by topological defects, Science 313 (5789) (2006) 954–958.
[4] Samo Kralj, Epifanio G. Virga, Slobodan Žumer, Biaxial torus around nematic point defects, Phys. Rev. E 60 (2) (1999) 1858.
[5] Yiwei Wang, Pingwen Zhang, Jeff Z.Y. Chen, Topological defects in an unconfined nematic fluid induced by single and double spherical colloidal particles, Phys. Rev. E 96 (4) (2017) 042702.
[6] Martin Robinson, Chong Luo, Patrick E. Farrell, Radek Erban, Apala Majumdar, From molecular to continuum modelling of bistable liquid crystal devices, Liq. Cryst. 44 (14–15) (2017) 2267–2284.
[7] T.C. Lubensky, D. Pettey, N. Currier, H. Stark, Topological defects and interactions in nematic emulsions, Phys. Rev. E 57 (1) (1998) 610.
[8] L. Onsager, The effects of shape on the interaction of colloidal particles, Ann. N.Y. Acad. Sci. 51 (1) (1949) 627–659.
[9] I. Bajc, F. Hecht, S. Žumer, A mesh adaptivity scheme on the Landau-de gennes functional minimization case in 3d, and its driving efficiency, J. Comput. Phys. 321 (2016) 981–996.
[10] D.W. Allender, G.P. Crawford, J.W. Doane, Determination of the liquid-crystal surface elastic constant K24, Phys. Rev. Lett. 67 (11) (1991) 1442.
[11] H. Kusumaatmaja, A. Majumdar, Free energy pathways of a multistable liquid crystal device, Soft Matter 11 (24) (2015) 4809–4817.
[12] J.K. Gupta, S. Sivakumar, F. Caruso, N.L. Abbott, Size-dependent ordering of liquid crystals observed in polymeric capsules with micrometer and smaller diameters, Angew. Chem., Int. Ed. 48 (9) (2009) 1652–1655.
[13] L. Zhang, Q. Du, Z.Z. Zheng, Optimization-based shrinking dimer method for finding transition states, SIAM J. Sci. Comput. 38 (1) (2016) A528–A544.
[14] G. Henkelman, H. Jónsson, A dimer method for finding saddle points on high dimensional potential surfaces using only first derivatives, J. Chem. Phys. 111 (15) (1999) 7010–7022.
[15] J.Y. Zhang, Q. Du, Shrinking dimer dynamics and its applications to saddle point search, SIAM J. Numer. Anal. 50 (4) (2012) 1899–1921.
[16] W.G. Gao, J. Leng, X. Zhou, Iterative minimization algorithm for efficient calculations of transition states, J. Comput. Phys. 309 (2016) 69–87.
[17] H. Jónsson, G. Mills, K.W. Jacobsen, Nudged elastic band method for finding minimum energy paths of transitions, in: Classical and quantum dynamics in condensed phase simulations, World Scientific, 1998, pp. 385–404.
[18] Q. Du, L. Zhang, A constrained string method and its numerical analysis, Commun. Math. Sci. 7 (4) (2009) 1039–1051.
[19] W.N. E, W.Q. Ren, E. Vanden-Eijnden, String method for the study of rare events, Phys. Rev. B 66 (5) (2002) 052301.
[20] W.N. E, W.Q. Ren, E. Vanden-Eijnden, Simplified and improved string method for computing the minimum energy paths in barrier-crossing events, J. Chem. Phys. 126 (6) (2007) 164103.
[21] W.Q. Ren, E. Vanden-Eijnden, A climbing string method for saddle point search, J. Chem. Phys. 138 (13) (2013) 134105.
[22] L. Lin, X.Y. Cheng, W.N. E, A.C. Shi, P.W. Zhang, A numerical method for the study of nucleation of ordered phases, J. Comput. Phys. 229 (5) (2010) 1797–1809.
[23] A. Samanta, M. Tuckerman, T.Q. Yu, W.N. E, Microscopic mechanisms of equilibrium melting of a solid, Science 346 (6210) (2014) 729–732.
[24] L. Zhang, L.Q. Chen, Q. Du, Morphology of critical nuclei in solid-state phase transformations, Phys. Rev. Lett. 98 (26) (2007) 265703.
[25] L. Zhang, L.Q. Chen, Q. Du, Simultaneous prediction of morphologies of a critical nucleus and an equilibrium precipitate in solids, Commun. Comput. Phys. 7 (4) (2010) 674.
[26] L. Zhang, W.Q. Ren, A. Samanta, Q. Du, Recent developments in computational modelling of nucleation in phase transformations, NPJ Comput. Mater. 2 (2016) 16003.
[27] Nigel J. Mottram, Christopher J.P. Newton, Introduction to q-tensor theory. arXiv, preprint, arXiv:1409.3542, 2014.
[28] Hiroyuki Mori, Eugene C. Gartland Jr, Jack R. Kelly, Philip J. Bos, Multidimensional director modeling using the q tensor representation in a liquid crystal cell and its application to the π cell with patterned electrodes, Jpn. J. Appl. Phys. 38 (1R) (1999) 135.
[29] Timothy A. Davis, Eugene C. Gartland Jr., Finite element analysis of the Landau-de Gennes minimization problem for liquid crystals, SIAM J. Numer. Anal. 35 (1) (1998) 336–362.
[30] B. Wincure, A.D. Rey, Growth and structure of nematic spherulites under shallow thermal quenches, Contin. Mech. Thermodyn. 19 (1–2) (2007) 37–58.
[31] F. Zernike, Diffraction theory of the knife-edge test and its improved form, the phase-contrast method, Mon. Not. R. Astron. Soc. 94 (1934) 377–384.
[32] V.N. Mahajan, G.M. Dai, Orthonormal polynomials in wavefront analysis: analytical solution, J. Opt. Soc. Am. A 24 (9) (2007) 2994–3016.
[33] D.C. Liu, J. Nocedal, On the limited memory BFGS method for large scale optimization, Math. Program. 45 (1–3) (1989) 503–528.
[34] A. Samanta, W.N. E, Optimization-based string method for finding minimum energy path, Commun. Comput. Phys. 14 (2) (2013) 265–275.
[35] T. Zhu, J. Li, A. Samanta, H.G. Kim, S. Suresh, Interfacial plasticity governs strain rate sensitivity and ductility in nanostructured metals, Proc. Natl. Acad. Sci. 104 (9) (2007) 3031–3036.
[36] P. Kaiser, W. Wiese, S. Hess, Stability and instability of an uniaxial alignment against biaxial distortions in the isotropic and nematic phases of liquid crystals, J. Non-Equilib. Thermodyn. 17 (1992) 153–170.
[37] S. Peled, H. Gudbjartsson, C.F. Westin, R. Kikinis, F.A. Jolesz, Magnetic resonance imaging shows orientation and asymmetry of white matter fiber tracts, Brain Res. 780 (1) (1998) 27–33.
[38] Z. Bradač, S. Kralj, M. Svetec, S. Žumer, Annihilation of nematic point defects: postcollision scenarios, Phys. Rev. E 67 (5) (2003) 050702.
[39] Y.C. Hu, Y. Qu, P.W. Zhang, On the disclination lines of nematic liquid crystals, Commun. Comput. Phys. 19 (2) (2016) 354–379.
[40] G. de Luca, A.D. Rey, Point and ring defects in nematics under capillary confinement, J. Chem. Phys. 127 (10) (2007) 104902.
[41] I.L. Ho, Fluctuation-induced non-equilibrium transition in a liquid-crystal metastable system, Physica A, Stat. Mech. Appl. 391 (5) (2012) 1952–1962.